TASK QUARTERLY 16 No 3–4, 173–184

DEFORMATION MEASUREMENT OF FLEXIBLE BIRDLIKE AIRFOIL WITH OPTICAL FLOW

XIAOLIANG GONG[1] AND STEPHAN BANSMER[2]

[1] *Northwestern Polytechnical University, 710072 Xi'an, China*
xlianggong@gmail.com

[2] *Technische Universität Braunschweig, 38108 Braunschweig, Germany*

(Received 9 April 2012; revised manuscript received 29 June 2012)

Abstract: The application of the Lucas-Kanade (LK) optical flow technique has seen a huge success in a wide variety of fields. The goal of this paper is to apply the Lucas-Kanade technique in measuring the deformation of flexible birdlike airfoil due to steady aerodynamic loads at transitional low Reynolds-numbers with a single pixel resolution. A pyramidal scheme is used to implement a coarse-to-fine warping strategy to allow large displacements. A nonlinear structure tensor is employed to diffuse local data anisotropically to preserve discontinuities in the optical flow field. Median filtering is introduced after each iteration to remove outliers. The upper surface of the airfoil is sprayed with stochastic ink dot pattern for easy capture by two cameras observed from two different angles above the airfoil to create a pattern on the airfoil for the deformation measurement. Finally, a general result of wind tunnel experiments is selected, two optical flow fields are calculated on two images generated from each camera respectively, and the optical flow results are compared with the image correlation results.

Keywords: optical flow, flexible airfoil deformation, pyramidal Lucas-Kanade, nonlinear structure tensor, image correlation

1. Introduction

1.1. Flapping flight

Over a million different species of insects fly with flapping wings to produce lift and thrust, and more than 10 000 different kinds of birds and bats flap their wings for locomotion [1]. Apparently, the insuperable maneuverability and agility of flapping flight contributes to their evolutionary success. Although flapping flight is much more complex than fixed or rotary winged flight, there has been continuous and substantial interest in it since the very beginning of the humans' dream of

flying like the birds, which has flourished abundant theoretical, experimental and numerical results over the past few decades.

1.2. Airfoil deformation

In some cases, the flexibility of flapping wings can increase both the thrust coefficient and the propulsive efficiency [2], which is a result of complex force interactions between aerodynamic forces, elastic forces and inertial forces. Indeed, the maximum camber during one flapping stroke has been found to vary from 8 to 12% [3]. Thus, in order to reveal the hidden mechanism behind these aeroelastic interactions and verify the numerical simulation based upon different assumptions, the measurement of model deformation has been of interest for quite many years. These techniques include videogrammetry [4], and projection moiré interferometry (PMI) [5]. However, videogrammetry is limited to measurement in sparse points no matter whether by retro-reflective targets [6] or projected coded targets, and PMI requires that the surface of interest be diffused. In this paper, we attempt to take the advantage of the optical flow to take the deformation measurement of an airfoil.

1.3. Optical flow

The optical flow determines the velocity field of two-dimensional image intensity motions with a single-pixel resolution. There are two main methods: global intensity smoothing methods based on the Horn-Schunck scheme [7], and local methods based on the Lucas-Kanade scheme [8]. Both methods are based on the assumption that the intensity of moving pixels is constant over a short duration, which is known as the brightness constancy assumption. This assumption results in the famous optical flow constant equation. Nevertheless, this single equation is insufficient to recover the velocity field, which is the well-known aperture problem. To solve this problem, the Horn-Schunck scheme assumes that the optical flow globally varies smoothly with the neighboring pixels that have nearly identical velocities, while the Lucas-Kanade scheme assumes that the optical flow is locally constant with the neighboring pixels in the same window sharing a similar motion. Accordingly, Horn-Schunck calculates a 100% density flow and it is sensitive to noise. Lucas-Kanade, on the other hand, does not give a dense flow but offers relatively high robustness under noise [9].

Since the Lucas-Kanade optical flow method was first proposed in 1981, it has been developed into numerous variants and the most widely used technique in computer vision [10]. The application of such a method has seen a huge success in a wide variety of fields. This paper applies the pyramidal Lucas-Kanade scheme [11] in the measurement of the deformation of a flexible birdlike airfoil due to steady aerodynamic loads at transitional low Reynolds-numbers.

1.4. Calibration

Combined with a calibration, it is possible to transform the optical flow information into a three-dimensional deformation of the airfoil. The pinhole model

and the polynomial model [12] are the two calibration models having been widely used, and the former has been used a lot in the Computer Vision community while the latter has often been used in the PIV community. As the image correlation calculated by Davis Software of LaVision uses a modified polynomial model, we also used it in the optical flow calibration for consistency. Another reason for using the polynomial model is that it is much easier to solve parameters in the polynomial model by the least square equation than to solve external parameters and internal parameters in the pinhole model.

2. Optical flow technique

Let $I_1(x, y, t)$ denote 2D image intensity, where x and y are the location of local intensity and t is the present time. Let $I_2(x+\mathrm{d}x, y+\mathrm{d}y, t+\mathrm{d}t)$ denote local intensity after short time duration where $\mathrm{d}t$ is the displacement of local intensity. The goal of the Lucas-Kanade scheme is to minimize the squared error in the integration window w:

$$E(\mathrm{d}x, \mathrm{d}y) = \min \sum_{x,\, y \in w} \left[I_1(x, y, t) - I_2(x+\mathrm{d}x, y+\mathrm{d}y, t+\mathrm{d}t)\right]^2 \tag{1}$$

After performing the first order Taylor expansion on $I_2(x+\mathrm{d}x, y+\mathrm{d}y, t+\mathrm{d}t)$, Equation (1) is simplified to:

$$E(\mathrm{d}x, \mathrm{d}y) = \min \sum_{x,\, y \in w} \left(I_x \mathrm{d}x + I_y \mathrm{d}y + I_t \mathrm{d}t\right)^2 \tag{2}$$

In our case, only two consequent images are considered, so we set $\mathrm{d}t$ equal 1. Then $\mathrm{d}x$, $\mathrm{d}y$ can be replaced with u, v, respectively. Equation (2) can be rewritten into:

$$E(u, v) = \min \sum_{x,\, y \in w} \left(I_x u + I_y v + I_t\right)^2 \tag{3}$$

A minimum of E with homogeneous Neumann (reflecting) the boundary condition satisfies $\partial_u E = 0$ and $\partial_v E = 0$, leading to a linear system:

$$\begin{bmatrix} \sum\limits_{x,\, y \in w} I_x^2 & \sum\limits_{x,\, y \in w} I_x I_y \\ \sum\limits_{x,\, y \in w} I_x I_y & \sum\limits_{x,\, y \in w} I_y^2 \end{bmatrix} \begin{bmatrix} u \\ v \end{bmatrix} = \begin{bmatrix} -\sum\limits_{x,\, y \in w} I_x I_t \\ -\sum\limits_{x,\, y \in w} I_y I_t \end{bmatrix} \tag{4}$$

At first sight, it is quite easy to solve this linear system. However, in practice this task can be trapped in a dilemma. There are three difficulties. First, the system matrix can be singular. Such singular matrices would appear in two regions, one is the homogeneous region where intensity derivatives are close to zero, leading to two near-zero eigenvalues; the other is around edges where one spatial derivative predominates, leading to a smaller eigenvalue being close to zero. Normally, we can threshold out these 'bad' regions by measuring the eigenvalues [13]. In our code, a small positive constant is added to the diagonal of the matrix to suppress too small eigenvalues which can be considered as 'noise'. Secondly, as all the pixels within a local window share the same velocity, this tends to blur discontinuities in the optical flow field. We draw ideas from [14] to utilize

a nonlinear structure tensor to preserve the flow discontinuities. Thirdly, the linearization of an essentially nonlinear problem maintains a proper accuracy only for quite a small displacement, say less than one pixel. With larger displacements, the pyramidal Lucas-Kanade method renders a reasonable result. It downsamples the original image with the factor 0.5 on each level and starts the optical flow computation at the coarsest image. The coarse solution is used as initialization for solving a refined image until the full resolution image is solved step by step [11]. At last, the median filter was introduced at the end of each iteration to discard outliers. It was originally proposed by [15] in particle image velocimetry (PIV) postprocessing to detect spurious vectors. It was also proved to improve optical flow result significantly [16].

3. Experimental setup

3.1. Wind tunnel

The experiments were carried out at the low-speed Low-Noise Wind Tunnel, see Figure 1. The inlet of the Eiffel-type tunnel is covered by a fleece mat 30mm in thickness. Afterward, the air passes through a straightener made of aluminum honeycombs, 14mm in diameter and 200mm in length, and then finally through a fine-mesh woven screen. In the large settling chamber, the small-scale turbulence is dissipated, and a Boerger-type nozzle contracts the air at a $16:1$ ratio. Consequently, the air has a very low turbulence level in the 400×600 millimeter sized test section. The wind tunnel is driven by a 4kW, acoustically encapsulated, speed controlled three-phase asynchronous motor, which produces stable wind-tunnel speeds from 2 up to 20 meters per second. The diffuser is mounted on a rail system, which allows interchanging modular test sections. The laboratory is lined with open-celled acoustic foam.

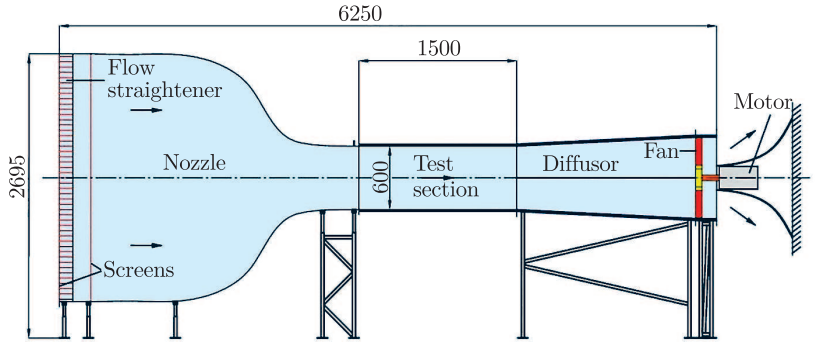

Figure 1. Schematic of the low-speed Low-Noise Wind Tunnel (dimensions in mm)

3.2. Airfoil

The flexible airfoil used in this paper is the birdlike airfoil SG04 [17], see Figure 2. It has been designed as a birdlike airfoil with two-dimensional behavior to study the coupled problem where the airfoil surface deformation is caused by

aerodynamic and inertial loads. The dot pattern on the upper surface is stochastic ink spray for easy capture of airfoil motion by camera. The movement of this stochastic dot pattern and hence the airfoil deformation is computed with the optical flow.

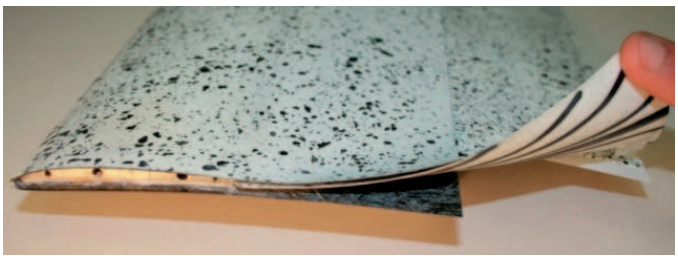

Figure 2. Flexible airfoil

3.3. Camera setup

The detailed camera setup is sketched in Figure 3 as a side view of the wind-tunnel test section. The left oncoming air flows over the flexible airfoil with a certain angle of attack. When the oncoming air flow is stable, the airfoil will be deformed. The Programmable Timing Unit (PTU9 by LaVision) is used to control a flash lamp to illuminate the airfoil, and two cameras in a stereoscopic setup to photograph the ink pattern on the upper surface of the airfoil. This procedure is repeated with the gradually increasing angle of attack, from 0 to 10 degrees, and gradually increasing the free stream velocity, from 0m/s to 8m/s. At last, we get two image series of the ink pattern for both cameras at a different experimental status. After that we apply the pyramidal Lucas-Kanade optical flow algorithm to the two image series respectively to calculate two optical flow fields, *i.e.* the displacement of ink patterns.

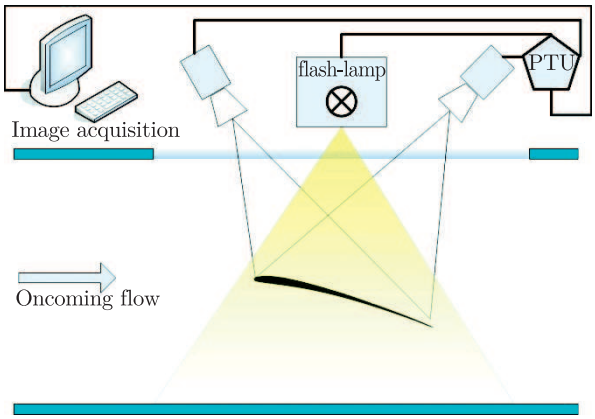

Figure 3. Custom-made deformation measurement system setup

4. Data evaluation

4.1. Insight into optical flow result

The synthetic sphere sequence [18] was selected to demonstrate the utility of our optical flow code. The sphere is rotating in the image sequence, while the background remains constant, see Figure 4. The true flow field of this sequence is known, which makes the verification of the optical flow much easier and more persuasive. Another more essential reason is that the spinning sphere consists of not only velocity regions having sharp discontinuities and continuous changes, but also image intensity having different discontinuous and continuous regions as velocity. This makes it possible for us to test the velocity discontinuity preserving the property of the nonlinear structure tensor in intensity discontinuity regions, and to see what would happen when there were velocity discontinuity in the smooth intensity region or vice versa. An initial result is shown by a color coded map in Figure 4. The hue represents the orientation of the vector and the brightness stands for its magnitude. The result is not identical to the true optical flow field, however, the preservation of discontinuity can be observed very well. But why are there several small slats cross the boundary in a periodical way? And why does the worse situation happen at the top right corner?

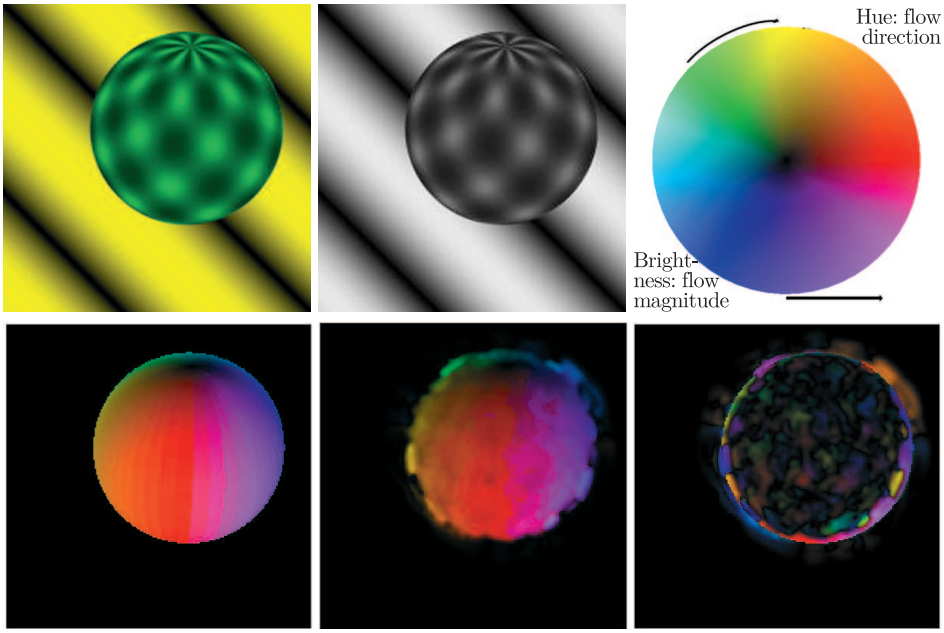

Figure 4. Top left: original sphere sequence (frame 1200×200 pixels); top middle: gray sphere sequence; top right: color code map; bottom left: ground truth flow field; bottom middle: optical flow field; bottom right: error flow field

The sphere sequence is a color image, however, since the camera used in our experiments provides only gray images, for consistency, the nonlinear structure

tensor takes into consideration the image gray difference only. Thus, the above mentioned defect is predictable. Looking carefully at these places, we can find that the grayscale intensities within the ball are quite similar to their corresponding background neighbors. Inside the ball, the optical flow result is not smooth which can be explained by noticeable gray value discontinuities. However, if we set up the experiment carefully, the problems discussed here can be avoidable, which can be demonstrated by the following comparison between the image correlation and the optical flow.

4.2. 2D flow field by optical flow and image correlation

A small square region (200×200 pixels) was extracted from the original image (1024×1280 pixels) captured by camera one to preliminiarily verify the optical flow, see Figure 5. The trailing edge of the airfoil can be seen on the left. The image correlation result is shown in Figure 6. Again, the optical flow result is coded by a color map, see Figure 7.

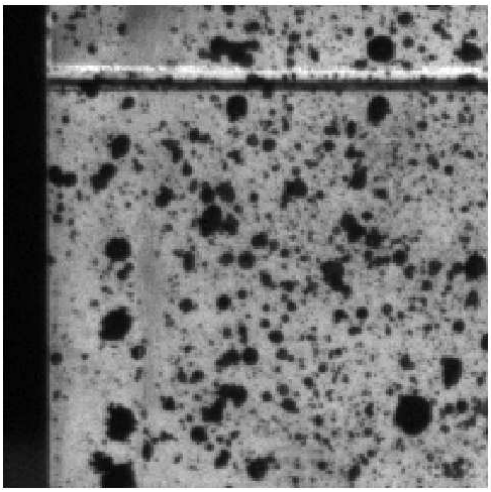

Figure 5. Extracted airfoil

The optical flow field captures left sharp discontinuity, benefiting from the fact that the image intensity and vector velocity share the same left boundary. The velocity within the extracted airfoil is smoother than that in the sphere. This is because most of the discontinuous regions inside the airfoil are in much smaller scale with respect to the scale of the airfoil. However, some discontinuous regions still affect the result.

Since the image correlation result gives an averaged flow vector over an area of 32×32 pixels, the correlation method is more insensitive to noise. The optical flow gives out a flow field with a single pixel resolution.

The comparison is done in three ways: angular error (AE), standard deviation of angular error (SD) and endpoint error (EE).

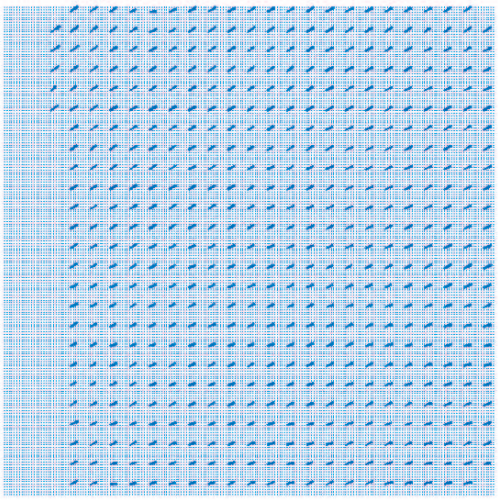

Figure 6. Image correlation 2D flow field

Figure 7. Optical flow field

AE was introduced by [13], and it is the most commonly used measure of performance for optical flow. The AE is calculated by measuring the angular difference between an estimated velocity $v_e = (u_e, v_e, 1)$ and the correct velocity $v_c = (u_c, v_c, 1)$:

$$\mathrm{AE} = \arccos\left(\frac{u_c u_e + v_c v_e + 1}{\sqrt{u_c^2 + v_c^2 + 1}\sqrt{u_e^2 + v_e^2 + 1}}\right) \tag{5}$$

Large and small velocities are treated without amplification as an innate property of the angular difference measurement. And AE can also handle the „divide by zero" problem for zero flows. SD is a standard deviation of AE.

Sometimes it is desirable to compute the EE used by Otte and Nagel [19], when we want that errors in a region of large velocities are weighted more than errors in a region of small velocities. EE is defined as follows:

$$\mathrm{EE} = \sqrt{(u_c - u_e)^2 + (v_c - v_e)^2} \tag{6}$$

According to the book on PIV by Raffel [20], our correlation result uncertainty is around 0.02 pixels. Here we assume that the image correlation result is the correct velocity v_c, and then we compare it with our optical flow result. The results of the aforementioned three comparison methods can be seen in Table 1. All these results confirm the consistency between the image correlation result and the optical flow result.

Table 1. Comparison between the PIV and optical flow

Measurement way	Error value
AE	4.3°
SD	2.87°
EE	0.10 pixel

4.3. Wing deformation by optical flow and image correlation

For the present study, we selected the case at the angle of attack $\alpha = 8°$. Two images from two cameras are at 0 m/s, and the other two are at 8 m/s (which correspond to the investigated Reynolds number of 10 000), see Figure 8, top. Then, the pyramidal Lucas-Kanade method was applied to the two images from each camera, after that, two optical flow fields were generated respectively, see Figure 8, bottom. The velocity range (in pixels) for camera one is: $u_1 \in (-0.8, 3.5)$, $v_1 \in (-4.7, 1.9)$. The velocity range for camera two is: $u_2 \in (-21.0, 6.8)$, $v_2 \in (-5.3, 3.7)$. In this paper, except for median filtering, no other postprocessing was used on the optical flow result.

Sharp discontinuities were captured well, including three straight lines representing the gaps between overlapping flexible shells. Since the ink spray in the middle part of the airfoil is much sparser compared with the left flexible shells, apparent wrinkled patterns or black holes can be observed in the middle region while the left region is relatively smoother.

Then, the calibration based on the polynomial model was carried out. The polynomial has cubic dependence in x and y, but quadratic dependence in z. The calibration grid was inclined with the same angle of the chord line of the airfoil, and was translated into three z-positions with an interval of 10 mm, containing the whole airfoil deformation range.

After calibration, we could reconstruct the 3D velocity field from the 2D optical flow field. However, as the SG04 airfoil behaves in a 2D way, the vertical deformation predominates in 3D displacements. This vertical deformation contour of the wing is shown in Figure 9, top left. A curve displaying the

vertical displacement of the airfoil can be plotted out, with a slice along the flow streamline, see Figure 9, top right.

In order to verify the optical flow result, stereoscopic cross-correlation was done using a multipass interrogation scheme with decreasing the interrogation window size (from 128×128 pixels down to 32×32 pixels), 50% overlap and elliptical weighting function. The vertical deformation contour and vertical displacement along the chord line can be seen in Figure 9, bottom.

On the one hand, the optical flow result and the image correlation result share several common features. First of all, all figures show that the near-zero deformation of the forebody is clear, which is in agreement with the airfoil design using carbon-reinforced plastic with a stiff forebody [17]. Secondly, from deformation contours, it has been shown that the wing deforms equally in the spanwise direction. Thirdly, an exponential-like increment follows the undeformed region, reaching a highest value around 3.8mm at the trailing edge. This deformation is considerable, regarding its scale and the low wind speed. Hence, the wing flexibility should influence the aerodynamic properties to a considerable extent, which will be studied in future in the following research. Finally, looking carefully at two vertical deformation curves along the chord line,

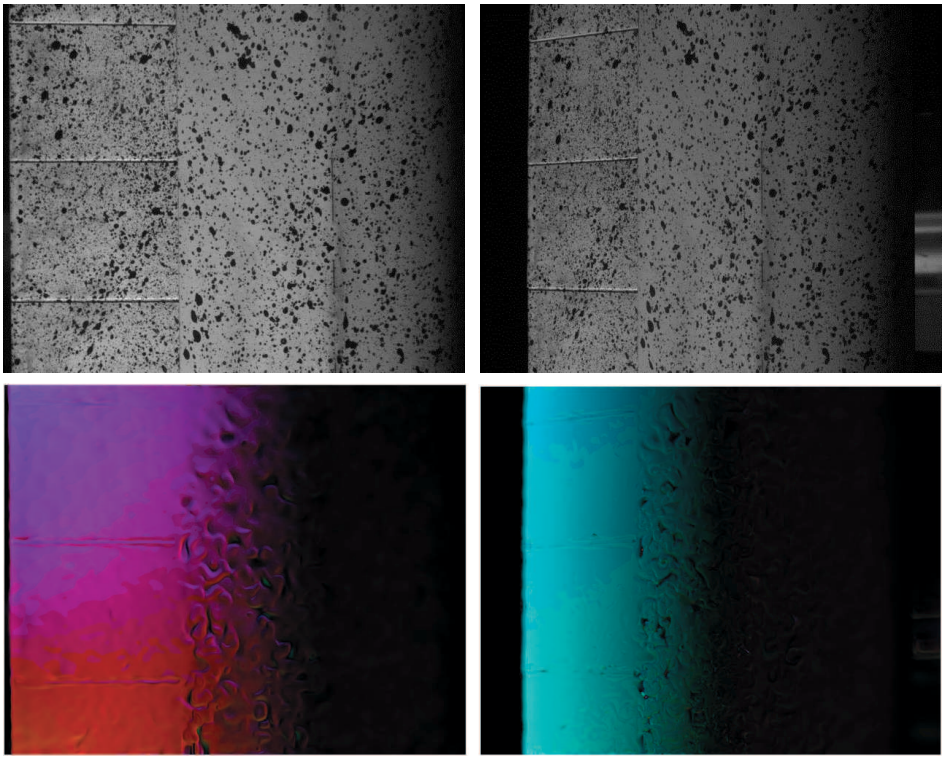

Figure 8. Top left: image from camera one, 0m/s, $\alpha = 8°$; top right: image from camera two, 0m/s, $\alpha = 8°$; bottom left: 2D optical flow from camera one; bottom right: 2D optical flow from camera two

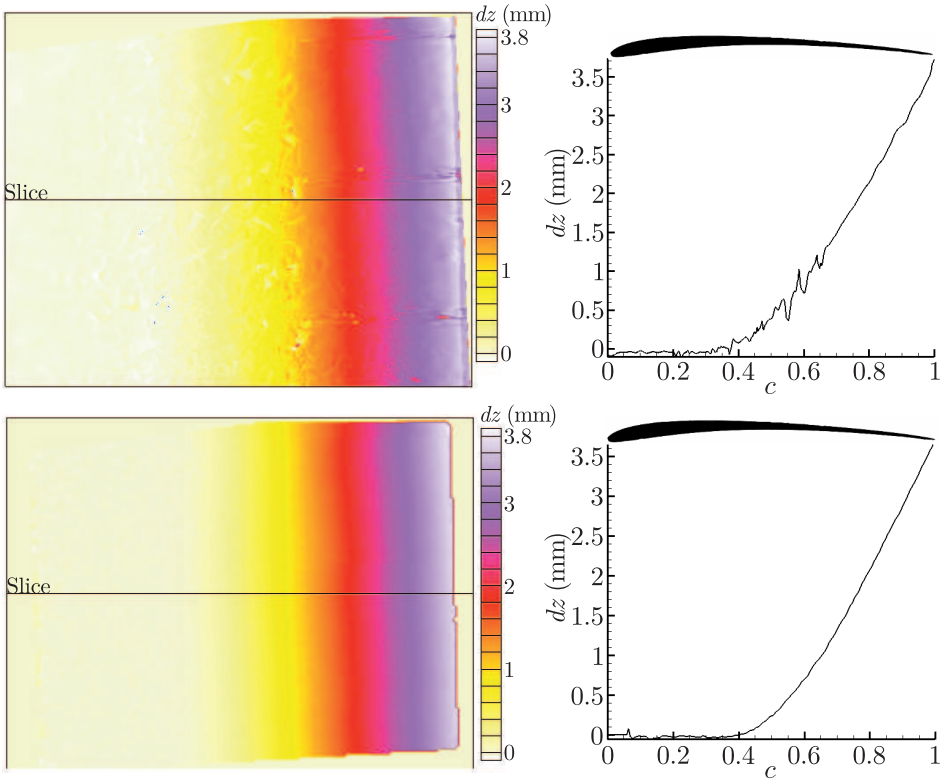

Figure 9. Left: vertical deformation contour of the 2D wing; right: vertical deformation curve along the chord line; top: optical flow result; bottom: image correlation result

Figure 9, left, we can find that both curves experience oscillation to a certain degree when the value is close to zero while both of them are smooth when the deformation is large, more precisely, above 1.2mm. Thus, both methods cannot accurately compute deformation which is too small (around zero). For large deformation, both methods handle well.

On the other hand, the optical flow result and the image correlation result have one obvious difference. Both the deformation contour and curve show that the optical flow fails to give a satisfactory smooth result in the middle part of the airfoil for the above discussed reason, that the ink spray pattern in this part is too sparse. It should not be surprising that the image correlation method could generate a smooth result since it used the interrogation window size starting from 128×128 pixels which is, of course, large enough to ignore the ink spray defect.

5. Conclusion

In this paper, a preliminary study on the deformation of a flexible birdlike wing by the pyramidal Lucas-Kanade optical flow method was done. The introduction of a nonlinear structure tensor contributes to the perservation of velocity discontinuity regions where the image intensity is also discontinuous. The flexible

airfoil was marked with a stochastic ink pattern. A stereoscopic camera setup was used to capture the motion of this pattern and thus the deformation of the airfoil. The pattern motion was well resolved with the present optical flow code. At last, the deformation of the birdlike wing was measured by stereoscopic image correlation and reconstructing the three-dimensional deformation from the optical flow. It was shown that the wing deformed equally in the spanwise direction. The deformation at the trailing edge at an angle of attack of 8 degree was determined to 3.8mm. The image correlation gave a smoother result than the optical flow, which was due to the sparse ink spray and the imperfect optical flow method. Nevertheless, the correlation scheme is limited in its spatial resolution by the size of the interrogation windows, 32×32 pixels in the present case. The optical flow code gives out a single pixel resolution. Further research will be done in the future in order to improve the optical flow result in the sparse pattern region. And a more precise 3D reconstruction from the 2D optical flow field will be studied as well.

References

[1] Dial K P 1994 *Report the Aerospace Profession, 38th Symposium Proceedings*, The Beverly Hilton, Beverly Hills, CA

[2] Heathcote S and Gursul I 2007 *AIAA J.* **45** (5) 1066

[3] Biesel W, Butz H and Nachtigall W 1985 *Biona-Report* **3** 139

[4] Johnson J T, Hughes S and Dam J V 2009 *J. ASME – Early Career Technical* **8** (1) 1

[5] Burner A W, Fleming G A and Hoppe J C 2000 *38th AIAA Aerospace Sciences Meeting and Exhibit*, Reno, Nevada, AIAA 2000-0835

[6] Barrows D A 2007 *45th AIAA Aerospace Sciences Meeting and Exhibit*, Reno, Nevada, AIAA 2007-1163

[7] Horn B K P and Schunck B C 1981 *Artificial Intelligence* **I7** 185

[8] Lucas B and Kanade T 1981 *Proc. Int. Joint Conf. Artificial Intelligence*, pp. 674–679

[9] Bruhn A, Weickert J and Schnörr C 2005 *Int. J. Computer Vision* **61** (3) 211

[10] Baker S and Matthews I 2004 *Int. J. Computer Vision* **56** (3) 221

[11] Bouguet J 2000 *Pyramidal Implementation of the Lucas Kanade Feature Tracker*, OpenCV Documentation, Intel Corporation, Microprocessor Research Labs

[12] Soloff S M, Adrian R J and Liu Z C 1997 *Meas. Sci. Technol.* **8** 1441

[13] Barron J L, Fleet D J and Beauchemin S S 1994 *Int. J. Computer Vision* **12** (1) 43

[14] Brox T and Weickert J 2002 *Lecture Notes in Computer Science*, Springer, Berlin, **2449** 446

[15] Westerweel J 1993 *Exp. Fluids* **16** 236

[16] Wedel A, Pock T, Zach C, Cremers D and Bischof H 2008 *An Improved Algorithm for TV-L1 Optical Flow*, in Dagstuhl Motion Workshop

[17] Bansmer S, Radespiel R, Unger R, Haupt M and Horst P 2010 *AIAA J.* **48** (9) 1959

[18] Galvin B, McCane B, Novins K, Mason D and Mills S 1998 *Proc. 1998 British Machine Vision Conf.*, Southampton, England

[19] Otte M and Nagel H-H 1994 *Proc. Eur. Conf. Computer Vision*, pp. 51–60

[20] Raffel M, Willert C and Kompenhans J 1998 *Particle Image Velocimetry, a Practical Guide*, Springer, Berlin, Heidelberg, New York, pp. 134–145